J. Coat. Technol. Res., **20** (1) 15–26, 2023
https://doi.org/10.1007/s11998-022-00661-7

Reaction-driven solvent transport in UV-curable phase-separating coatings

M. Yamamura

Received: 29 January 2022 / Revised: 5 May 2022 / Accepted: 8 May 2022
© The Author(s) 2022

Abstract We experimentally examined the time-evolutions of local compositions in photocurable, monomer-solvent-initiator ternary liquid film coatings using attenuated total-reflectance-Fourier transform infrared spectroscopy. The coatings exhibited phase separation upon UV exposure owing to the inherent partial miscibility between the solvent and the polymer. The solvent concentration at the bottom of the coating increased when exposed to UV light for 1 s from the top, showing a solvent transport along the irradiation direction. The differences in solvent concentration before and after UV exposure showed good agreement with model predictions based on stress-induced non-Fickian solvent mass transport. The solvent concentrations at the bottom remained constant in the case of discrete phase structures, whereas it exponentially decayed over time in bicontinuous phase structures. These results suggest that light-tunable microstructures enable the relaxation of the reaction-driven nonuniformity in solvent concentration distributions.

Keywords UV curing, Phase separation, Liquid thin film, Reaction-diffusion coupling

Supplementary Information The online version contains supplementary material available at https://doi.org/10.1007/s11998-022-00661-7.

This paper was presented at the 14th European Coatings Symposium held in 2021 in Brussels, Belgium.

M. Yamamura (✉)
Department of Applied Chemistry, Kyushu Institute of Technology, Sensui 1-1, Tobata, Kitakyushu, Fukuoka, Japan
e-mail: yamamura@che.kyutech.ac.jp

Introduction

Ultraviolet (UV) curing technology has been widely used in the coatings industry to produce optical,[1] protective,[2] flame-retardant,[3] and super-hydrophilic[4] thin film coatings. Typical examples of reactants include polyester acrylate,[5] polyurethane acrylate,[6,7] and other reactive monomers or oligomers. Consider a liquid film consisting of photoreactive monomers and photoinitiator molecules. Upon exposure to UV light, the photoinitiator molecules absorb the light to generate radicals that react with the monomers and promote chain reactions to create polymers. Light attenuation in a liquid can produce depth-wise gradients in the degree of cure.[8] The nonuniform profile of monomer-to-polymer conversion propagates from the illuminated surface toward the unpolymerized area as a traveling wave,[9–11] referred to as frontal photopolymerization (FPP). When the polymerization reactions locally consume the reactant in the photo-irradiated area, the unreacted monomers diffuse against the direction of light irradiation.[12,13] In a mixture of monomers with different reactivities, the highly reactive monomers diffuse toward the exposed area,[14,15] whereas the components with low reactivity are extruded from the exposed area,[16] leading to spatial variations in composition.[17] The reactions also induce stresses during the development of polymer networks that span across the film and transform the liquid into an elastic or viscoelastic solid.[18–22] It is of scientific and practical importance to elucidate the formation mechanism of spatial nonuniformities in compositions across the coating thickness. A fundamental understanding of these reaction-diffusion couplings is critical not only in coating applications but also in roll-to-roll micromolding,[23] 3D printing,[24] and photolithography of microfluidic devices.[25]

However, the reaction-diffusion couplings in curable liquids containing non-reactive, incompatible solvent

have received little attention. When the solvent chosen is immiscible or partially miscible with the reaction products, the solvent-monomer-polymer phase diagram shows a two-phase region, in which the liquid is no longer thermodynamically stable.[26] The trajectory of liquid compositions enters the two-phase regime when the degree of polymerization increases beyond a critical value during the curing process (Fig. 1a). Consequently, the liquid undergoes phase separation into solvent-rich and polymer-rich domains by either spinodal decomposition (SD) in an unstable state or nucleation and growth (NG) in a metastable state. The two-phase region expands on the phase diagram and thus phase separation kinetics vary as increasing the difference in solubility parameters between the solvent and the polymer. Furthermore, when the conversion profiles propagate along the direction of light, as in solvent-free coatings, the traveling conversion front may be followed by a secondary front that divides the nonseparating and phase-separating layers (Fig. 1b), which increases the complexity of the spatiotemporal evolution of local compositions.

This nonequilibrium curing process in the presence of a solvent, herein referred to as frontal photo-induced phase separation (fPIPS), has received considerable attention as a promising route for the fabrication of battery separators and precision filters as it enables the creation of light-tunable, submicron-scale pores in cured films by subsequent evaporation from solvent-rich domains.[27,28] Viklund et al.[29] prepared molded macroporous polymer monolith utilizing monomer mixtures of trimethylolpropane trimethyacrylate and 2,3-epoxypropyl methacrylate and porogenic solvents of toluene and 2,2,4-trimethylpentane. Yu et al.[30] examined the photo polymerization of a mixture of ethylene dimethacrylate, butyl meth-acrylate, and 2-acrylamido-2-methyl-1-propanesulfonic acid in a mixture of 1-propanol, 1,4-butanediol, and water. Courtois et al.[31] investigated photopolymerizations of 2,3-epoxypropyl methacrylate in the presence of poly(ethylene glycol) as a porogen and sixteen different solvents as co-porogens under either continuous or pulsed UV light exposure. Yu et al.[32] compared porous structures prepared from different porogenic solvents, methanol and decanol, which have different degrees of solubility for hydroxyethyl methacrylate and ethylene glycol dimethacrylate monomers. Elsner et al.[33] utilized a mixture of 1-dodecanol, 2–propanol, and toluene as a porogenic solvent and fabricated 3D microstructures with different feature sizes. Ma et al.[34] adopted photo-initiated thiol-yne polymerization to fabricate monoliths within a capillary by using a binary porogenic system of diethylene glycol diethyl ether/poly(ethylene glycol). Recently, Korzhikova-Vlakh and Tennikova[35] systematically examined Hansen's solubility parameter distances between monomers and porogenic solvents and showed good linear relationships between measured average pore sizes with the predicted parameter distances. However, the underlying diffusion mechanisms remain poorly understood. According to Yoshihara,[27] UV exposure from the top surface led to solvent enrichment at the bottom of photocuring coatings in the absence of evaporation, demonstrating the light-driven, anomalous solvent transport. Despite the progress in physical modeling of reaction-induced phase separation[36–38] as well as experimental investigations for thermally-cured phase-separating epoxy systems,[39–41] to the best of our knowledge, few studies have attempted to explain the reasons why solvent molecules diffuse during the curing of coatings, and how the coupling between photo-reactions, stress development, and phase separation impact the diffusion behavior of the solvent.

In this paper, we examined the time evolutions of local compositions in photocurable liquid film coatings containing a nonreactive solvent. Attenuated total reflectance-Fourier transform infrared (ATR-FTIR)

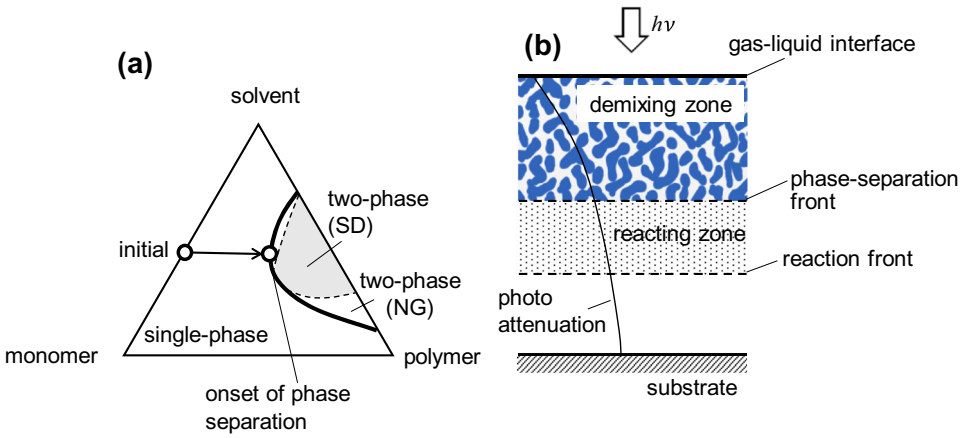

Fig. 1: (a) Schematic phase diagram of a monomer-polymer-solvent ternary system at a given photoinitiator concentration. (b) Schematic cross section of a coating exhibiting a frontal photo-induced phase separation (fPIPS). Directional photo-irradiation creates nonuniform composition profiles with the traveling reaction/phase-separation fronts across the thickness

spectroscopy showed that the solvent concentration at the bottom of the coating increased when exposed to UV light for 1 s from the top. Model predictions based on stress-induced non-Fickian solvent mass transport agreed with the measured values for a range of high initial monomer contents. Static light scattering experiments revealed the development of phase-separated microstructures in as-exposed films. The solvent concentration at the bottom remained constant in island-sea structures, but exponentially decayed over time in bicontinuous phase structures. These findings suggest that photopolymerization reactions induce nonuniform solvent concentration profiles that are subsequently relaxed by molecular diffusion when inter-connected, phase-separated domains develop across the thickness. The present work differs from our previous publication,[42] which examined multicomponent solution drying before UV curing. It also differs from reference (28) which focused on the development of a novel measurement technique to determine local concentration distributions of polymerized and unpolymerized monomers. This study sheds new light on the reaction-diffusion interplay in phase-separating photocurable coatings and, to the best of our knowledge, provides the first quantitative explanation for the non-Fickian transport of solvent along the direction of light.

Experimental procedure

Materials

We used phenylbis (2,4,6-trimethlybensoyl-)phosphine oxide (Irg819, BASF) as the photoinitiator, polyester-acrylate (Aronix-M9050, Mw=1000–1500, Toagosei) as the photoreactive monomer, and methylethylketone (MEK, Wako Chemical) as the solvent. The monomer-to-initiator mass ratio in the ternary solutions was fixed at 9 w/w, while the solvent concentration ranged between 0.2 and 1.0 g-MEK/g-solutes. The chemicals were used as purchased, without further purification. The photoinitiator (Irg819) and the acrylate monomer (Aronix-M9050) used in this work are commercially available and applicable to practical reactive systems that require relatively high glass transition temperatures after curing.[43] The relative amount of initiator, i.e., the mass ratio of initiator to monomer was chosen not to exceed the solubility limit of the initiator but to be high enough to achieve monomer conversions higher than 20% when the sample was exposed to UV light for 1 s. We have previously utilized 1,3 α-alkyl amino phenone (Irgacure 379 EG; BASF) as initiator and explored formation mechanism of submicron-scale pores[27] and nonuniform concentration distributions[28] in M9050 solution systems. We here chose Irg819 as one of the common initiators that have been used to examine photo-polymerization reaction kinetics.[44,45]

Attenuated total reflectance-Fourier transform infrared (ATR-FTIR) analysis

A predetermined volume of the solution was ejected from a pipette and coated onto the ZnSe prism of the ATR-FTIR spectrophotometer (IRAffinity-1 with MIRAcle 10, Shimadzu). The coated area was set as 1 cm^2 by attaching a 2 mm thick silicone shim on the prism stage. The liquid volume was adjusted to form 200 or 600 μm thick solution films. A transparent cover glass was attached to the shim surface to minimize solvent evaporation during the measurements. An LED UV light source (HSL-50UV365-4UTK, CCS) with a wavelength of 365 ± 5 nm was set on top of the prism surface at a distance of 8.7 cm. The UV intensity on the prism surface was measured by a power meter (C6060-365-03, Hamamatsu) and regulated between 5 and 45 mW/cm^2. To promote photopolymerization reactions, the closed solution sample was exposed to UV light for 1 s, mimicking high-speed roll-to-roll processing at substrate speeds of ∼ 120 m/min. The experimental procedure is schematically shown in Fig. 2a. We needed 2–3 s (2.7 s on average) to collect spectrum data within 700–1500 cm^{-1} and a resolution of 4 cm^{-1}. To examine the time-evolutions of the spectra, we conducted multiple shot data collections by repeating the same data acquisition procedure to obtain spectra every 2–3 s.

To determine the local compositions in the vicinity of the solution-prism interface, we built calibration curves using the IR spectra of ternary solutions with known concentrations. We observed three distinct absorption peaks at 808, 981, and 1363 cm^{-1} associated with the out-of-plane C-H bending vibrations on C=C double bonds in polyester-acrylate; unreactive C-O bonds in polyester-acrylate; and the symmetric stretching of CH_3 bonds in MEK, respectively. We employed a cubic function of the normalized absorbance ratio with respect to the solvent mass fraction (c): $A_{1363}/A_{981} = a_0 + a_1\, c + a_2\, c^2 + a_3\, c^3$, where A_λ is the absorbance at wavelength λ. The constants a_0–a_3 were obtained by linear functions with respect to the Irg819 mass fraction (p) as $a_i = m_i\, p + n_i$ (i = 0–3). The constants m_i and n_i are listed in Table 1. The absorbance ratio calculated by the cubic function agreed with the measurements with the errors between -2% and 6% in the concentration range of $0 < c < 0.6$, as illustrated in the Supporting Information (Fig. S1). The monomer-to-polymer conversion is defined as the amount of polymerized monomers relative to the initial amount of monomer. This is expressed as $\gamma = 1 - (A_{808}/A_{981})^t/(A_{808}/A_{981})^0$, where the superscripts 0 and t represent the absorbance ratio before irradiation and the time after the start of photo-irradiation, respectively.

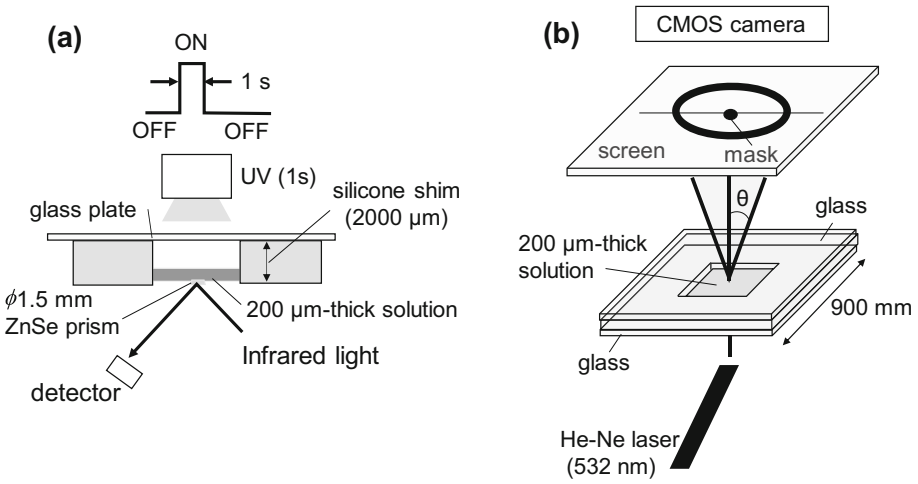

Fig. 2: Schematics of experimental procedures of (a) attenuated total reflectance-Fourier transform infrared (ATR-FTIR) measurements and (b) light scattering measurements

Table 1: Material constants to express A_{1363}/A_{981} as a cubic function with respect to the solvent mass fraction

i	m_i	n_i
0	9.68×10^{-3}	0.139
1	3.46	1.05
2	− 16.2	− 0.536
3	38.7	4.70

Scanning electron microscopy

The surface structures of dried films were characterized by scanning electron microscopy (SEM, S-4800, Hitachi High Technologies) as follows. First, the ternary solution was coated onto an 1.1 mm thick glass plate instead of the ZnSe prism using the same procedure mentioned above. Then, the sample film was dried at room temperature by opening the glass cover, peeled off from the substrate, washed with ethanol to remove unreacted monomers, and further dried in vacuum before SEM imaging.

Light scattering analysis

To identify whether phase separation proceeds via an SD or NG mechanism, a TEM00-mode He-Ne laser (Edmond) with a wavelength of $\lambda = 532$ nm and a beam diameter of 5 mm was passed through the photo-irradiated wet film. The experimental procedure is schematically shown in Fig. 2b. The static light scattering pattern on a white screen was captured by a CMOS camera (WAT-01U2, Wantec) as a digital image. RGB image decomposition was applied to each image using ImageJ software. The green (G) values of each pixel were extracted from three different lines that crossed the center of the photomask. For photo-cured samples with low solvent concentration, the line profiles of the G values were broad with no distinct peaks at any radial position, indicating the formation of discrete, island-sea-type phase structures created via the NG mechanism. In contrast, at higher solvent concentrations, the scattering pattern exhibited the maximum in intensity at a certain critical radial coordinate r_m, which is associated with the bicontinuous phase structure created by the SD mechanism. We determined the scattering angle corresponding to the intensity peak, $\theta_m = \tan^{-1}(r_m/L)$, where L denotes the distance between the sample and screen. Our preliminary measurements revealed that no apparent porous structure developed below the dry thickness of 36 μm at the solvent concentration of 1.0 g-MEK/g-solutes and the UV intensity of 30 mW/cm^2. Typical examples of raw scattering patterns at different solvent concentrations of u = 0.8 and 0.2 g-MEK/g-solutes, corresponding to SD and NG patterns, respectively, are shown in the Supporting Information (Fig. S2a and S2b).

Results and discussion

Figure 3a shows the SEM image of a dried coating surface. The solution was exposed to UV light with an intensity of 30 mW/cm^2 and wavelength of 365 ± 5 nm for 1 s. The initial solvent concentration and initial wet thickness were 1.0 g-MEK/g-solutes and 200 μm, respectively. Photo-irradiation led to the formation of irregular-shaped fine pores with a longitudinal length of 50 nm and a width of less than 20 nm. The static light scattering experiment revealed a ring-shaped pattern for the same wet sample, indicating the occurrence of periodic composition fluctuations with a characteristic length scale[46] typically created by the SD mechanism. The pattern evolved immediately after UV irradiation

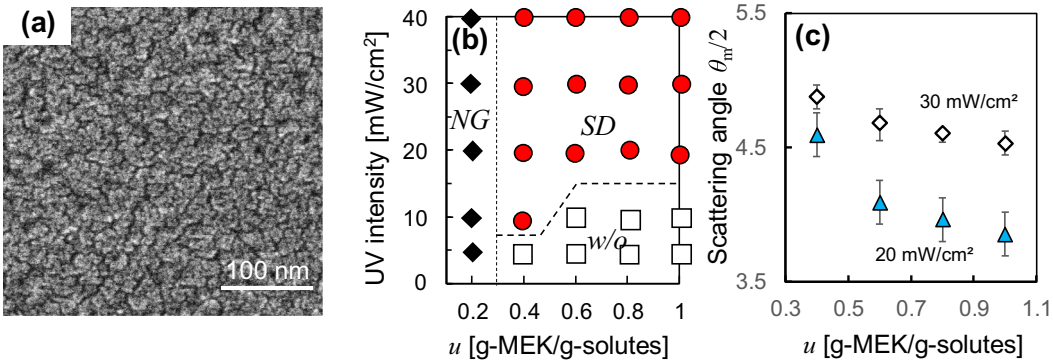

Fig. 3: (a) SEM image of a cured film with an initial solvent concentration (*u*) of 1.0 g-MEK/g-solutes and the initial thickness of 200 μm. The solution was irradiated with UV light with an intensity of 30 mW/cm^2 and wavelength of 365 ± 5 nm for 1 s. Then, the film was dried at room temperature and washed by ethanol to remove residual monomers, leaving irregular-shaped pores on the top surface. (b) Phase-separation regime map based on the initial solvent concentration (*u*) and the light intensity of irradiation. The spinodal decomposition (SD, closed circle) and nucleation and growth (NG, closed diamond) regimes were identified from the line profiles of scattering intensity with a peak at a certain scattering angle, and a broad profile with no distinct peak, respectively. No scattering image was observed at low light intensities and high solvent concentrations, implying macroscopically homogeneous films without phase-separated domains (open rectangle). (c) Variations in the scattering angles (θ_m) in the SD regime with the solvent concentrations at light intensities of 20 and 30 mW/cm^2. The scattering angle decreased with increasing solvent concentration, indicating that the sizes of phase structures are tunable by the initial compositions. The dry thickness was approximately 56 μm at the initial solvent content of 0.2 g-MEK/g-solutes

and was maintained for 60 s. This implies that the phase separation over time was stopped by the rapid polymerization reactions, which quickly froze the phase-separated microstructures in a nonequilibrium state. We collected the scattering data at different initial solvent concentrations and photointensities, and summarized the results in a phase regime map, as shown in Fig. 3b. Bicontinuous phase structures created by the SD mechanism (closed circle) developed in the regime with high light intensities and solvent concentrations, whereas discrete, island-sea structures created by the NG mechanism (closed diamond) developed in the regime with solvent concentrations below a critical value. The decrease in light intensity at a given concentration yielded homogeneous coatings without phase structures, as shown in the figure. It is worth noting that the domain size was tunable by changing the solvent concentration in the SD regime. As shown in Fig. 3c, the scattering angle $(\theta_m/2)$ increased, and hence the characteristic length scale of the separated phases $(1/|q|)$ decreased, with decreasing the initial solvent concentrations at a given light intensity, where $|q|$ denotes the scattering vector of $|q| = 4\pi/\lambda \cdot \sin(\theta_m/2)$. The angle θ_m further increased with the increase in light intensity.

Figure 4 shows the typical examples of ATR-FTIR spectra of 200 μm thick ternary solution films at wavelengths of (a) 800–820 and (b) 1355–1370 cm^{-1} and UV intensities of 0, 5, and 40 mW/cm^2. The spectra with a resolution of 4 cm^{-1} were collected at 2.7 s after the start of UV exposure. The liquid consisted of the monomer, initiator, and solvent with a mass ratio of M9050/ Irg819/MEK = 9/1/4. The absorbance of 808 cm^{-1}—associated with the out-of-plane C-H bending vibrations on C=C double bonds in polyester-acrylate molecules—decreased with increasing light intensity, suggesting that the amount of unreacted monomer decreased as the polymerization reactions proceeded. The monomer-to-polymer conversion calculated from the spectra was $\gamma = 0.340$. Our preliminary measurements showed that the conversion reached 0.6 under continuous photo-irradiation for 20 s (not shown here), and reached 0.9 in methyl isobutyl ketone.[27] This implies that the relatively low conversion in the present study is due to the limited amounts of active radicals generated during the short photo-irradiation time. On the other hand, the increase in light intensity increased the absorbance of 1363 cm^{-1} associated with the symmetric stretching of CH_3 bonds in MEK molecules. This indicates that the solvent concentration increased near the coating bottom surface of photocured films.

In the second series of FTIR measurements, we varied the initial solvent concentration while fixing the photointensity at 40 mW/cm^2. To quantify how photo-irradiation changes the solvent bottom concentration, the absorbance-concentration calibration curves were adapted for each spectrum measured before and 2.7 s after UV exposure. As shown in Fig. 5a, the change in bottom concentration of the solvent (Δc) first increased, reached a peak at a critical concentration (u_c), and then decreased with increasing initial solvent concentration in photocurable liquids. A similar trend was observed in the monomer-to-polymer conversions (γ), implying that the variation in solvent concentration is directly related to the photopolymerization reactions. This phenomenon is qualitatively similar to that in previous studies demonstrating the extrusion of a low-reactive monomer from the exposed area in

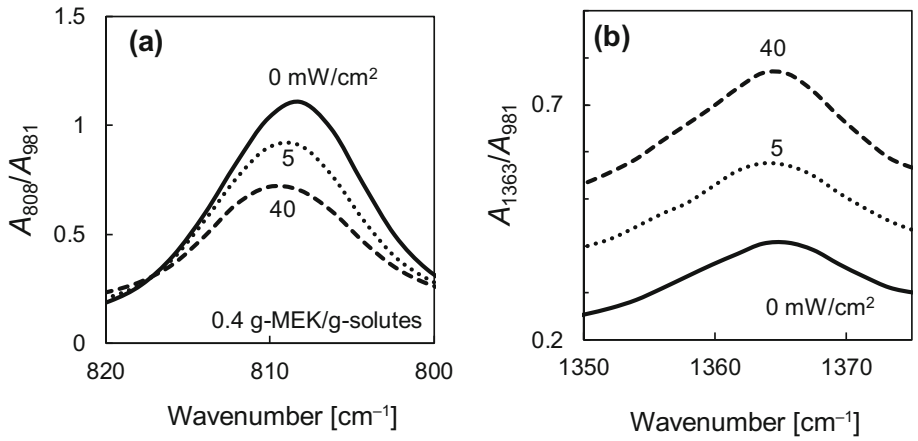

Fig. 4: ATR-FTIR spectra of 200 μm thick ternary solution films of M9050/ Irg819/MEK = 9/1/4 (w/w) near the absorption peaks at (a) 808 and (b) 1363 cm^{-1} associated with the out-of-plane C–H bending vibrations on C=C double bonds in polyester-acrylate, and the symmetric stretching of CH_3 bonds in MEK, respectively. The films were exposed to UV light with a wavelength of 365 ± 5 nm for 1s to collect the spectra obtained at 2.7 s. The absorbance of 808 cm^{-1} decreased with increasing light intensity, whereas that of 1363 cm^{-1} increased with increasing light intensity. This suggests that polymerization reactions induced the diffusion of the solvent toward the bottom surface of the coating. The absorbance was normalized at 981 cm^{-1}, which is associated with the vibration of unreactive C-O bonds in the polyester-acrylate

mixtures of monomers with different reactivities.[15–17] The low conversions at solvent contents above u_c may be attributed to the fact that the monomer molecules are less likely to encounter radicals in diluted liquids. On the other hand, concentrated monomer solutions showed significant photoattenuation that reduced the conversion. Figure 5b shows the transmittance predicted by Beer's law for 200 μm thick solution films at a wavelength of 365 nm. The monotonic decrease in transmittance with decreasing solvent concentration indicates that the irradiated light was preferentially absorbed near the top coating surface; hence, it hardly contributes to the reactions at the coating bottom.

To explain why the solvent concentration was increased by UV irradiation, we considered stress-induced solvent transport along the direction of light. Stress began to develop with the growth of polymer networks spanning across the coating to show elasticity.[47,48] The photocuring coating shrank freely in the thickness direction but was constrained in the plane of the coating, leading to the development of in-plane stresses.[49,50] The stress no longer relaxed but rather contributed to non-Fickian solvent mass transport when the characteristic relaxation time of the polymer was sufficiently long compared to that of solvent diffusion [51, and references therein]. According to Vinjamur and Cairncross,[51] the change in solvent concentration is proportional to that of the stress when the stress evolution is expressed by the Maxwell model with a sufficiently long relaxation time. The stresses squeezed out solvent molecules from the exposed area, inducing a mass flux of solvent toward the bottom coating surface.

To gain better physical insights, we built a simple model of solvent transport by considering the reaction-induced strain $(h_0 - h)/h_0$, where h_0 and h denote the thickness before and after the light exposure, respectively. For simplicity, we assumed that only the top layer with thickness h_0-h was subjected to strain, while the underlying bottom layer maintained the initial concentrations of the monomer and the photoinitiator. When all solvent molecules at the top layer were squeezed out by stress to form a solvent-rich bottom layer with a uniform concentration profile and thickness of h_0-h, the mass balance gives the solvent mass fraction in the bottom layer as $c = 2c_0/(1+c_0)$, where c_0 is the initial solvent mass fraction. Therefore, the variations in the solvent bottom concentration before and after light exposure is expressed as $\Delta c = c_0\,(1-c_0)/(1+c_0)$. The solid curve in Fig. 5 represents the model predictions, which first increased, reached a maximum of Δc_{max} = 17.2 wt%, and then decreased with increasing solvent concentration. The predicted and measured values showed good agreement in the low concentration regimes of u < 0.6 g-MEK/g-solutes, indicating that the model captures the experimental trends in a qualitative sense. However, the model overestimated the measurements at higher solvent contents, at which bicontinuous phase structures developed in the cured films (see Fig. 3b).

We systematically conducted similar spectroscopic measurements under different operating conditions to summarize the variations in solvent concentration difference with respect to the monomer-to-polymer conversions (Fig. 6). We varied the initial solvent concentrations between 0.2 and 1.0 g-MEK/g-solutes, while the monomer-to-initiator mass ratio and film thickness were fixed at 9 w/w and 200 μm, respectively. High light intensities of 20 (triangles), 30 (diamond), and 40 (circles) mW/cm^2 were chosen to promote phase separation at any solvent concentration of interest. The increase in conversion led to a monotonic

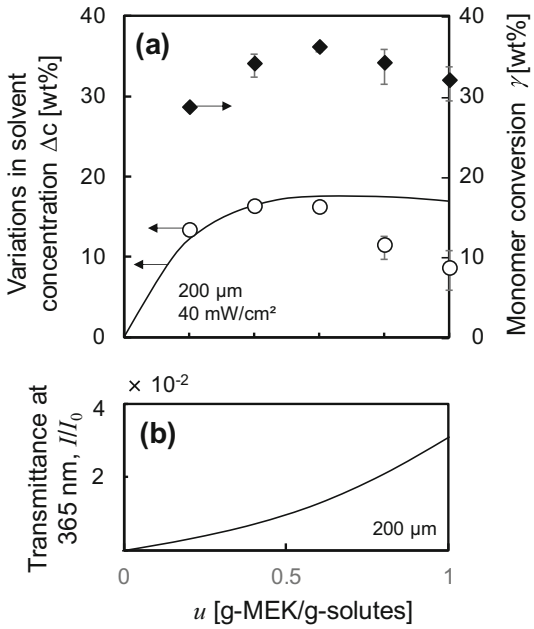

Fig. 5: (a) Variations in solvent bottom concentrations before and after UV exposure (Δc) and monomer-to-polymer conversions (γ) with the initial solvent concentration. In photocurable liquids, the solvent concentration first increased and then decreased with increasing initial solvent concentration. The solid curve in the figure represents the model predictions, which showed good agreement with the measurements at low concentration regimes. The monomer conversion exhibited a peak at a solvent concentration of ~ 0.6 g-MEK/g-solutes. (b) Transmittance predicted from the Beer's law for 200 μm thick solution films at the wavelength of 365 nm. The increase in solvent concentration resulted in a monotonic increase in transmittance. The absorption coefficient of the photoinitiator was determined as 15.1 wt%$^{-1}$cm^{-1} by preliminary UV-Vis spectroscopy measurements, and used for the prediction. The absorption coefficients of the solvent and monomer were negligibly small compared with those of the initiator

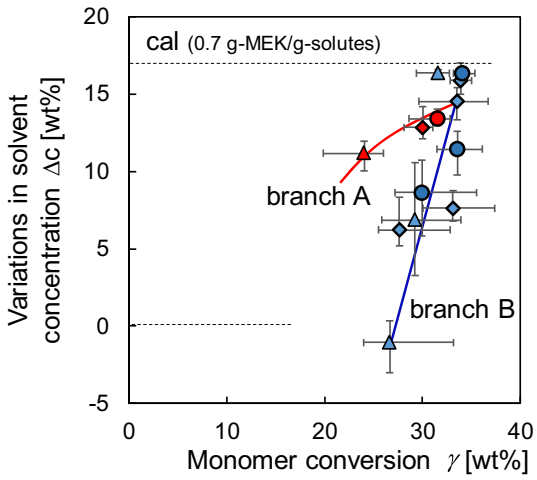

Fig. 6: Effect of average monomer-to-polymer conversion on the solvent concentration difference before and 2.7 s after the UV irradiation of different intensities of 20 (▲), 30 (◇), and 40 (○) mW/cm^2, respectively. The solvent concentrations ranged between 0.2 and 1.0 g-MEK/g-solutes, while the monomer-to-initiator mass ratio and the film thickness were fixed at 9 w/w and 200 μm, respectively. The solvent concentration difference (Δc) was negligibly small at low conversions. An increase in conversion split the Δc into two branches, A and B, corresponding to cases in which the coatings developed island-sea and bicontinuous phase-separated structures, respectively. The measured data converged into a band on each branch at different UV light intensities and liquid compositions. The solid lines are the guide to the eye

increase in the solvent concentration, suggesting that the photopolymerization reactions governed the transport of solvent via reaction-diffusion coupling. The measured data was split into two branches regardless of the initial solvent concentration and UV intensity. The light scattering measurements revealed that the two branches, A and B, correspond to the conditions in which the coatings developed island-sea and bicontinuous phase structures, respectively.

The A-branch is located at a higher concentration level compared to the B-branch for a range of low conversions. The model prediction (Δc_{max}, broken line in Fig. 6) showed good agreement with the measured values at the high γ limit where the two branches meet each other.

To explain the physical reasons why the bicontinuous and discrete phase structures exhibit different diffusion behaviors of the solvent, we conducted time-resolved IR spectroscopy measurements. Figure 7 shows the time evolutions in (a) monomer-to-polymer conversion and (b) the solvent concentration difference before and after UV exposure (Δc) at initial solvent concentrations of 0.2 and 0.8 g-MEK/g-solutes. The conversion jumped into a higher value during the short UV exposure period and remained almost constant even after the light was turned off, showing quantitatively the same trend in both phase structures (Fig. 7a). However, the diffusion kinetics of the solvent differed after the initial increases: the solvent bottom concentration remained constant in the case of island-sea structures, and it monotonically decreased over time in the coating with bicontinuous phase structures (Fig. 7b). The broken lines in Fig. 7b represent the model predictions at initial solvent concentrations of 0.2 and 0.8 g-MEK/g-solutes, corresponding to c_0 = 0.16 and 0.44. The difference between the predicted and measured concentrations was negligible within a certain experimental error at a low solvent content, but significantly increased over time in the case of high solvent content.

These results show that (i) nonuniform solvent distributions develop in UV-curable films upon light exposure. (ii) This nonuniformity subsequently relaxes via *backward* diffusion against the direction of light. (iii) A structural transition from bicontinuous to discrete phases hinders the diffusional relaxation. The

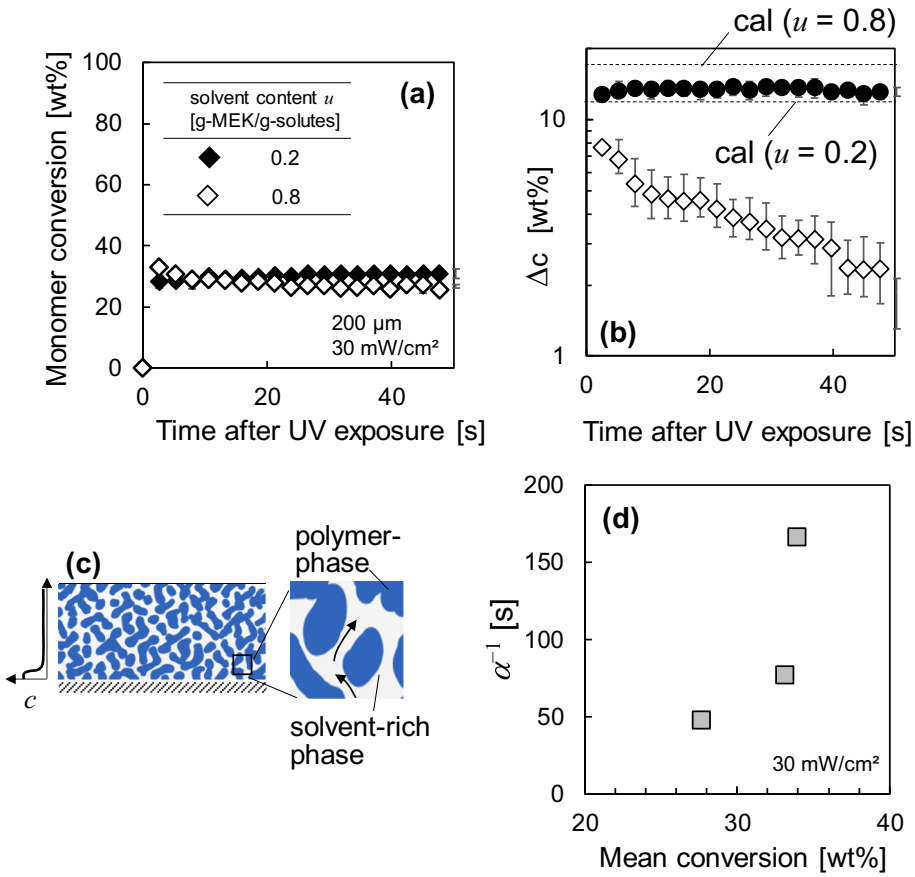

Fig. 7: Time evolutions in (a) monomer-to-polymer conversion and (b) the solvent concentration difference before and after the UV exposure (Δc) at initial solvent concentrations of 0.8 and 0.2 g-MEK/g-solutes, at which bicontinuous and island-sea phase structures developed in the films, respectively. The local solvent concentration at the coating bottom monotonically decreased over time in the former, whereas it retained almost a constant value in the latter case, despite no significant difference in the conversions. (c) Schematic cross-sectional illustration of a phase-separating liquid in which solvent-rich phases function as effective channels for the backward solvent transport from the bottom film surface. (d) Variations in the characteristic time-scale (a^{-1}) for solvent diffusion with respect to the monomer conversion measured at 2.7 s after light exposure. The measured Δc over time obeyed an exponential function $\Delta c \sim \exp(-at)$ when the bicontinuous phase structures developed. The increase in conversion resulted in a monotonic increase in the time scale, indicating that the backward diffusion of the solvent slowed down at higher conversions. The monomer-to-initiator mass ratio, UV intensity, and the film thickness were fixed at 9 w/w, 30 mW/cm^2, and 200 μm, respectively

backward diffusion of the solvent is explained as follows. When the polymerization reactions quench the solution system into a thermodynamically unstable state, infinitely small compositional fluctuations spontaneously grow to reduce the free energy of mixing, undergoing SD that creates tortuous, interconnected domain structures of either solvent-rich or polymer-rich phases. More detailed descriptions for the phase separation is shown in the Supporting Information (Fig. S3). The SD front, i.e., the border between the reacting (yet not separating) and phase-separating layers, propagates across the thickness toward the coating bottom, where solvent molecules were accumulated by stress-induced non-Fickian transport. Subsequently, the SD front meets the bottom coating surface to trigger the solvent diffusion through the phase-separated layer. Because the solvent-rich phases involve larger hole-free-volumes, and thus lower diffusive resistances compared with polymer-rich domains, the solvent-rich phases act as effective continuous channels for molecular diffusion, guiding solvent transport away from the coating bottom (Fig. 7c). In contrast, few diffusion channels can develop in island-sea phase structures when solvent-rich domains are discretely distributed in polymer-rich matrices. The nonuniform solvent concentration distributions are no longer relaxed but remain for a certain period of time, giving rise to a solvent-rich layer that remains within the vicinity of the bottom coating surface. This physical picture is consistent with the fact that the transition from branch A to B in Fig. 6, i.e., from island-sea to bicontinuous phase structures,

decreased the solvent concentration at a given conversion. This hypothesis allows us to explain why the model prediction that neglects the relaxation in concentration gradients overestimates the measurements when bicontinuous phase structures develop at high solvent concentrations of $u > u_c$ (Fig. 5a).

Figure 7b also reveals that the measured variations in solvent bottom concentrations obey an exponential function as $\Delta c \sim \exp(-at)$ where a^{-1} denotes the characteristic time-scale for solvent diffusion. The exponential decay in concentration is consistent with the analytical solution of the governing equation for Fickian diffusion in a one-dimensional, stationary, quasi-binary liquid.[52] To further quantify the structure-dependent diffusivity, we fitted the data with an exponential function to obtain a constant a for each initial solvent concentration (u) of 0.4, 0.6, and 0.8 g-MEK/g-solutes. The phase structure remained bicontinuous at any u value of interest at a light intensity of 30 mW/cm^2. As illustrated in Fig. 7d, the increase in the monomer-to-polymer conversion resulted in a monotonic increase in a^{-1}, suggesting that the backward diffusion of solvent significantly slowed down with the growth of polymer networks in the films. The time-scale tends to be diverse at high conversions, possibly because the solvent diffusion coefficients were reduced by several orders of magnitude by the strong molecular interactions in the curing liquids.

From a practical viewpoint, the accumulation of solvent molecules at the bottom surface is sometimes undesirable because it may promote a decrease in evaporation rates, trapping skinning of the solvent,[51] curling[27] and/or delamination due to drying-induced stresses driven by the difference in strain between the top and bottom surfaces. Thus, it is important to understand (i) the physical origin of solvent localization and (ii) the relaxation mechanism of a nonuniform concentration profile to avoid the drying defects. The good agreement between the model predictions and measurements shown in Fig. 5 indicates that the stress-induce molecular transport is a source of the solvent localization in photocuring coatings. Figures 6 and 7 revealed that the bicontinuous phase structures assist the relaxation in solvent concentration gradients, showing the exponential decay in concentration with conversion-dependent relaxation times. The present results provide useful information for controlling asymmetric compositional profiles by tuning the degree of curing and microstructures developed in the coatings.

One might argue that the diffusion in photocuring coatings is influenced by the ratio between the liquid thickness (h) and the characteristic light penetration depth (h_c). We expect the variations in solvent bottom concentration to decrease when reaction/phase-separation fronts do not reach the bottom surface of the film because of the negligible intensity of transmitted light at $h/h_c >> 1$. To verify this hypothesis, we increased the solution film thickness to 600 μm while fixing the solvent concentration and light intensity as 0.2 g-MEK/g-solutes and 30 mW/cm^2, respectively. The results show that the solvent bottom concentration maintained its initial value throughout the spectroscopy measurements for 50 s (not shown here). The light penetration depth was h_c = 232 μm, above which the UV light transmittance falls below 0.01% at the bottom surface, as predicted by Beer's law using the predetermined molar absorption coefficient. These results indicate that the reaction-induced increase in solvent bottom concentration occurs only when the thickness is comparable to, or less than, the critical thickness associated with the light penetration depth.

We here emphasize that the coatings developed in the present study are potentially applicable to battery separators, supporting layers for membrane separation films, or scaffolds for tissue engineering because submicron-scale, interconnected porous structures of the coatings would be suitable for fast transports of ions and gasses across the thickness. Furthermore, the frontal photo-induced phase separation requires neither specially-synthesized chemicals or a time-consuming rinsing process to remove polymer-lean phases, showing a promising feature for direct applications for industrial roll-to-roll processing.

Further studies are needed to explore the transient reaction-diffusion interplays. Once photoinitiator molecules absorb light and generate radicals, the polymerization reactions proceed and the coating shrinks to promote stress-induced molecular transport, which in turn changes the reaction kinetics because the local compositions, and thereby the local light intensity, could vary at different time scales. The numerical modeling of coupled equations for reaction kinetics, photoattenuation, stress development, and multicomponent diffusions could provide better physical insights on how concentration/stress profiles propagate across the thickness. The complexity further increases in phase-separating systems where (i) local physical properties in each separating phase vary over time as the phases grow; (ii) stress evolution is dependent on phase morphologies[53]; and (iii) the two-phase region on a phase diagram expands with increasing polymer molecular weights. Although the results of the stress-induced diffusion model proposed in this study agreed with the measured data within a certain limited composition range, more rigorous models are needed to obtain a fundamental understanding of the reaction-diffusion coupling behavior in photocuring coatings containing solvent. In addition, measurements and/or predictions of mechanical properties of the phase-separated acrylic coatings may provide useful information for practical applications. We preliminarily attempted to examine tensile strengths of the photocured samples, but the coatings curled to a considerable extent after peeling off from the substrate, showing difficulties to prepare a specimen of suitable dimensions for the measurements. It is one of our future works to elucidate how the phase structures affect mechanical properties of the acrylic coatings

prepared by the frontal photo-induced phase separation processing, but it is beyond the scope of this study.

Conclusions

We examined the photopolymerization process of ternary solution coatings containing an acrylic monomer, a photoinitiator, and solvent. Upon UV exposure, the coatings exhibited phase separation into solvent-rich and polymer-rich domains, as verified by static light scattering experiments. Time-resolved ATR-FTIR measurements showed that photo-irradiation promoted the increase in solvent concentration at the bottom coating surface. The measured maximum concentration difference monotonically increased with increasing monomer-to-polymer conversion, and split into two separated branches, corresponding to conditions in which bicontinuous and discrete phase structures developed, regardless of the UV intensity and initial solvent concentration. The measured concentrations agreed well with the model predictions, assuming a stress-induced instantaneous solvent transport along the direction of light. However, the model overestimated the measurements when the cured coating involved bicontinuous phases associated with ring-shaped light scattering patterns. These results show that the nonuniform solvent concentration profile is initially created by reaction-induced stresses, but is then relaxed by molecular diffusion through the interconnected, phase-separated domains across the thickness.

Acknowledgment The author wishes to thank T. Ogata and Y. Kuroiwa for assistance with the experiments and Y. Mawatari and Y. Saito for fruitful discussions. The authors acknowledge the financial support of the Japan Society for the Promotion of Science (JSPS) KAKENHI (20H02507) Grant-in-Aid for Scientific Research B.

Open Access This article is licensed under a Creative Commons Attribution 4.0 International License, which permits use, sharing, adaptation, distribution and reproduction in any medium or format, as long as you give appropriate credit to the original author(s) and the source, provide a link to the Creative Commons licence, and indicate if changes were made. The images or other third party material in this article are included in the article's Creative Commons licence, unless indicated otherwise in a credit line to the material. If material is not included in the article's Creative Commons licence and your intended use is not permitted by statutory regulation or exceeds the permitted use, you will need to obtain permission directly from the copyright holder. To view a copy of this licence, visit http://creativecommons.org/licenses/by/4.0/.

References

1. Kourtakis, K, Bekiarian, P, Blackman, G, Lewittes, M, Subramoney, S, ''Novel Thermal and Photo Curable Anti-Reflective Coatings Using Fluoroelastomer Nanocomposites and Self-assembly of Nanoparticles.'' *J. Coat. Technol. Res.*, **13**, 753–762 (2016)
2. Nkeuwa, WN, Riedl, B, Landry, V, ''Wood Surfaces Protected with Transparent Multilayer UV-Cured Coatings Reinforced with Nanosilica and Nanoclay. Part II: Application of a Standardized Test Method to Study the Effect of Relative Humidity on Scratch Resistance.'' *J. Coat. Technol. Res.*, **11** (6) 993–1011 (2014)
3. Gu, Z, Nan, Y, Zhang, Y, Huang, J, Liu, J, ''Synthesis and Properties of Phosphorus-Containing Cardanol-Based Acrylates for Flame-Retardant UV/EB-Cured Coatings.'' *J. Coat. Technol. Res.*, **18** (5) 1353–1364 (2021)
4. Liang, T, Li, H, Lai, X, Su, X, Zhang, L, Zeng, X, ''A Facile Approach to UV-Curable Super-Hydrophilic Polyacrylate Coating Film Grafted on Glass Substrate.'' *J. Coat. Technol. Res.*, **13** (6) 1115–1121 (2016)
5. Kim, HK, Ju, HT, Hong, JW, ''Characterization of UV-Cured Polyester Acrylate Films Containing Acrylate Functional Polydimethylsiloxane.'' *Eur. Polym. J.*, **39** (11) 2235–2241 (2003)
6. Huang, J, Xiong, Y, Zhou, X, Yang, Z, Yuan, T, ''A Novel Polyfunctional Polyurethane Acrylate Prepolymer Derived from Bio-based Polyols for UV-Curable Coatings Applications.'' *Polym. Test.*, **106** 107439 (2022)
7. Tsupphayakorn-aek, P, Suwan, A, Tulyapitak, T, Saetung, N, Saetung, A, ''A Novel UV-curable Waterborne Polyurethane-Acrylate Coating Based on Green Polyol from Hydroxyl Telechelic Natural Rubber.'' *Prog. Org. Coat.*, **163** 106585 (2022)
8. Song, JO, McCormick, AV, Francis, LF, ''Depthwise Viscosity Gradients in UV-Cured Epoxy Coatings.'' *Macromol. Mater. Eng.*, **298** 145–152 (2013)
9. Terrones, G, Pearlstein, AJ, ''Effects of Optical Attenuation and Consumption of a Photobleaching Initiator on Local Initiation Rates in Photopolymerizations.'' *Macromolecules*, **34** 3195–3204 (2001)
10. Cabral, JT, Hudson, SD, Harrison, C, Douglas, JF, ''Frontal Photopolymerization for Microfluidic Applications.'' *Langmuir*, **20** 10020–10029 (2004)
11. Warren, JA, Cabral, JT, Douglas, JF, ''Solution of a Field Theory Model of Frontal Photopolymerization.'' *Phys. Rev. E. Stat. Nonlinear Soft Matter Phys.*, **72** 021801 (2005)
12. Hennessy, MG, Vitale, A, Matar, OK, Cabral, JT, ''Controlling Frontal Photopolymerization with Optical Attenuation and Mass Diffusion.'' *Phys. Rev. E Stat. Nonlinear Soft Matter Phys.*, **91** 062402 (2015)
13. Hennessy, MG, Vitale, A, Matar, OK, Cabral, JT, ''Monomer Diffusion into Static and Evolving Polymer Networks During Frontal Photopolymerisation.'' *Soft Matter*, **13** 9199–9210 (2017)
14. Sakaguchi, Y, Kawahara, K, Yamada, T, Okazaki, Y, Imahashi, S, ''Diffusion of Unreacted Monomers Detected by ATR FTIR Spectroscopy in a Photosensitive Printing Plate After the Photoreaction.'' *J. Appl. Polym. Sci.*, **92** 2903–2907 (2004)
15. Sánchez, C, de Gans, BJ, Kozodaev, D, Alexeev, A, Escuti, MJ, van Heesch, C, Bel, T, Schubert, US, Bastiaansen, CWM, Broer, DJ, ''Photoembossing of Periodic Relief Structures Using Polymerization-Induced Diffusion: A Combinatorial Study.'' *Adv. Mater.*, **17** 2567–2571 (2005)

16. Leewis, CM, de Jong, AM, van Ijzendoorn, LJ, Broer, DJ, ''Reaction-Diffusion Model for the Preparation of Polymer Gratings by Patterned Ultraviolet Illumination.'' *J. Appl. Phys.*, **95** 4125–4139 (2004)
17. Kragt, AJJ, Broer, DJ, Schenning, APHJ, ''Easily Processable and Programmable Responsive Semi-interpenetrating Liquid Crystalline Polymer Network Coatings with Changing Reflectivities and Surface Topographies.'' *Adv. Funct. Mater.*, **28** 1704756 (2018)
18. Payne, JA, Francis, LF, Mccormick, AV, ''The Effects of Processing Variables on Stress Development in Ultraviolet-Cured Coatings.'' *J. Appl. Polym. Sci.*, **66** 1267–1277 (1997)
19. Stolov, AA, Xie, T, Penelle, J, Hsu, SL, Stidham, HD, ''An Analysis of Photopolymerization Kinetics and Stress Development in Multifunctional Acrylate Coatings.'' *Polym. Eng. Sci.*, **41** 314–328 (2001)
20. Sun, G, Wu, X, Liu, R, ''A Comprehensive Investigation of Acrylates Photopolymerization Shrinkage Stress from Micro and Macro Perspectives by Real Time MIR-Photo-Rheology.'' *Prog. Org. Coat.*, **155** 106229 (2021)
21. Li, S, Sun, D, Li, A, Cui, Y, ''Study on Curing Shrinkage and Mechanism of DHOM-Modified Epoxy-Acrylate-Based UV-curing 3D Printing Materials.'' *J. Appl. Polym. Sci.*, **138** (7) 49859 (2021)
22. Roose, P, ''Residual Stress in Radiation-Cured Acrylate Coatings.'' *React. Funct. Polym.*, **73** (2) 323–331 (2013)
23. Du, Y, Jochem, KS, Thakral, N, McCormick, AV, Francis, LF, ''Roll-to-Roll Micromolding of UV Curable Coatings.'' *J. Coat. Technol. Res.*, **18** (3) 627–639 (2021)
24. Wang, D, Chen, T, Zeng, Y, Chen, X, Xing, W, Fan, Y, Qiao, X, ''Optimization of UV-Curable Alumina Suspension for Digital Light Processing of Ceramic Membranes.'' *J. Membr. Sci.*, **643** 120066 (2022)
25. Hamad, EM, Bilatto, SER, Adly, NY, Correa, DS, Wolfrum, B, Schöning, MJ, Offenhäusser, A, Yakushenko, A, ''Inkjet Printing of UV-Curable Adhesive and Dielectric Inks for Microfluidic Devices.'' *Lab Chip*, **16** 70–74 (2016)
26. Wang, L, Ding, Y, ''Creating Micro-Structured Hydrogel-Forming Polymer Films by Photo-Polymerization in an Evaporating Solvent: Compositional and Morphological Evolutions.'' *Eur. Polym. J.*, **66** 99–107 (2015)
27. Yoshihara, H, Yamamura, M, ''Formation Mechanism of Asymmetric Porous Polymer Films by Photoinduced Phase Separation in the Presence of Solvent.'' *J. Appl. Polym. Sci.*, **136** 47867 (2019)
28. Yoshihara, H, Yamamura, M, ''Concentration Profiles in Phase-Separating Photocuring Coatings.'' *J. Coat. Technol. Res.*, **16** 1629–1636 (2019)
29. Viklund, C, Pontén, E, Glad, B, Irgum, K, Hörstedt, P, Svec, F, '''Molded' Macroporous Poly(glycidyl methacrylate-*co*-trimethylolpropane trimethacrylate) Materials with Fine Controlled Porous Properties: Preparation of Monoliths Using Photoinitiated Polymerization.'' *Chem. Mater.*, **9** (2) 463–471 (1997)
30. Yu, C, Svec, F, Frechet, JMJ, ''Towards Stationary Phases for Chromatography on a Microchip: Molded Porous Polymer Monoliths Prepared in Capillaries by Photoinitiated In Situ Polymerization as Separation Media for Electrochromatography.'' *Electrophoresis*, **21** 120–127 (2000)
31. Courtois, J, Byström, E, Irgum, K, ''Novel Monolithic Materials Using Poly(ethylene glycol) as Porogen for Protein Separation.'' *Polymer*, **47** 2603–2611 (2006)
32. Yu, S, Ma, KCC, Mon, AA, Ng, FL, Ng, YY, ''Controlling Porous Properties of Polymer Monoliths Synthesized by Photoinitiated Polymerization.'' *Polym. Int.*, **62** (3) 406–410 (2013)
33. Elsner, C, Heinz, D, Prager, A, Knolle, W, Zimmer, K, ''Phase Separation Micromoulding and Photopatterning Based on Radiation Induced Free Radical Polymerisation of Acrylates for the Microfabrication of Porous Monolithic Structures.'' *J. Micromech. Microeng.*, **24** (9) 095002 (2014)
34. Ma, S, Zhang, H, Li, Y, Li, Y, Zhang, N, Ou, J, Ye, M, Wei, Y, ''Fast Preparation of Hybrid Monolithic Columns via Photo-Initiated Thiol-Yne Polymerization for Capillary Liquid Chromatography.'' *J. Chromatogr. A*, **1538** 8–16 (2018)
35. Korzhikova-Vlakh, EG, Tennikova, TB, ''Some Factors Affecting Pore Size in the Synthesis of Rigid Polymer Monoliths: Theory and Its Applicability.'' *J. Appl. Polym. Sci.*, **139** e51431 (2022)
36. Ohnaga, T, Chen, W, Inoue, T, ''Structure Development by Reaction-Induced Phase Separation in Polymer Mixtures: Computer Simulation of the Spinodal Decomposition Under the Non-isoquench Depth.'' *Polymer*, **35** (17) 3774–3781 (1994)
37. Li, C, Strachan, A, ''Coarse-Grained Molecular Dynamics Modeling of Reaction-Induced Phase Separation.'' *Polymer*, **149** 30–38 (2018)
38. Surendran, A, Joy, J, Parameswaranpillai, J, Anas, S, Thomas, S, ''An Overview of Viscoelastic Phase Separation in Epoxy Based Blends.'' *Soft Matter*, **16** (14) 3363–3377 (2020)
39. Jyotishkumar, P, Ozdilek, C, Moldenaers, P, Sinturel, C, Janke, A, Pionteck, J, Thomas, S, ''Dynamics of Phase Separation in Poly(acrylonitrile-butadiene-styrene)-Modified Epoxy/DDS System: Kinetics and Viscoelastic Effects.'' *J. Phys. Chem. B*, **114** (42) 13271–13281 (2010)
40. Vijayan, PP, Puglia, D, Kenny, JM, Thomas, S, ''Effect of Organically Modified Nanoclay on the Miscibility, Rheology, Morphology and Properties of Epoxy/Carboxyl-Terminated (Butadiene-co-acrylonitrile) Blend.'' *Soft Matter*, **9** 2899–2911 (2013)
41. Vijayan, PP, George, JS, Thomas, S, ''The Effect of Polymeric Inclusions and Nanofillers on Cure Kinetics of Epoxy Resin: A Review.'' *Polym. Sci. Series A*, **63** 637–651 (2021)
42. Yamamura, M, ''Drying Paths of Phase-Separating Solution Coatings Exposed to Humidity.'' *J. Coat. Technol. Res.*, **19** 15–23 (2022)
43. Gasa, JV, Balasubramani, PK, ''Low Temperature Curable Adhesive Composition and Articles Including the Same.'' *US Patent* 10,968,367 (2021)
44. Chibac, AL, Buruiana, T, Melinte, V, Mangalagiu, I, Epurescu, G, Buruiana, EC, ''Synthesis of New Photoactive Urethane Carbohydrates and Their Behavior in UV or Femtosecond Laser-Induced Two-Photon Polymerization.'' *Des. Monomers Polym.*, **19** (1) 12–23 (2016)
45. Buruiana, EC, Chibac, AL, Buruiana, T, Melinte, V, Balan, L, ''A Benzophenone-Bearing Acid Oligodimethacrylate and Its Application to the Preparation of Silver/Gold Nanoparticles/Polymer Nanocomposites.'' *J. Nanopart. Res.*, **15** 1335 (2013)
46. Hashimoto, T, Kumaki, J, Kawai, H, ''Time-Resolved Light Scattering Studies on Kinetics of Phase Separation and Phase Dissolution of Polymer Blends. 1. Kinetics of Phase Separation of a Binary Mixture of Polystyrene and Poly(viny1 methyl ether).'' *Macromolecules*, **16** 641–648 (1983)
47. Wu, J, Qian, Y, Sutton, CA, La Scala, JJ, Webster, DC, Sibi, MP, ''Bio-Based Furanic Di(meth)acrylates as Reactive Diluents for UV Curable Coatings: Synthesis and Coating Evaluation.'' *ACS Sustain. Chem. Eng.*, **9** (46) 15537–15544 (2021)

48. Bakhshandeh, E, Sobhani, S, Croutxé-Barghorn, C, Allonas, X, Bastani, S, ''Siloxane-Modified Waterborne UV-Curable Polyurethane Acrylate Coatings: Chemorheology and Viscoelastic Analyses.'' *Prog. Org. Coat.*, **158** 106323 (2021)
49. Jian, Y, He, Y, Jiang, T, Li, C, Yang, W, Nie, J, ''Volume Shrinkage of UV-Curable Coating Formulation Investigated by Real-Time Laser Reflection Method.'' *J. Coat. Technol. Res.*, **10** (2) 231–237 (2013)
50. Francis, LF, McCormick, AV, Vaessen, DM, Payne, JA, ''Development and Measurement of Stress in Polymer Coatings.'' *J. Mater. Sci.*, **37** 4717–4731 (2002)
51. Vinjamur, M, Cairncross, RA, ''Non-Fickian Non-Isothermal Model for Drying of Polymer Coatings.'' *AIChE J.*, **48** (11) 2444–2458 (2002)
52. Carslow, HS, Yaeger, JC, *Conduction of Heat in Solids*. Oxford University Press, New York (1986)
53. Vaessen, DM, McCormick, AV, Francis, LF, ''Effects of Phase Separation on Stress Development in Polymeric Coatings.'' *Polymer*, **43** 2267–2277 (2002)

Publisher's Note Springer Nature remains neutral with regard to jurisdictional claims in published maps and institutional affiliations.